RESEARCH ARTICLE

Rift kinematics preserved in deep-time erosional landscape below the northern North Sea

Thilo Wrona[1,2] | Alexander C. Whittaker[3] | Rebecca E. Bell[3] |
Robert L. Gawthorpe[1] | Haakon Fossen[4] | Christopher A.-L. Jackson[5] |
Marit Stokke Bauck[6,7]

[1]Department of Earth Science, University of Bergen, Bergen, Norway

[2]GFZ German Research Centre for Geosciences, Potsdam, Germany

[3]Department of Earth Science and Engineering, Imperial College, London, UK

[4]Museum of Natural History, University of Bergen, Bergen, Norway

[5]Department of Earth and Environmental Sciences, The University of Manchester, Manchester, UK

[6]CGG, Oslo, Norway

[7]Department of Geosciences, University of Oslo, Oslo, Norway

Correspondence

Thilo Wrona, GFZ German Research Centre for Geosciences, Telegrafenberg, 14473 Potsdam, Germany.
Email: wrona@gfz-potsdam.de

Abstract

Our understanding of continental rifting is, in large parts, derived from the stratigraphic record. This record is, however, incomplete as it does not often capture the geomorphic and erosional signal of rifting. New 3D seismic reflection data reveal a Late Permian-Early Triassic landscape incised into the pre-rift basement of the northern North Sea. This landscape, which covers at least $542\,km^2$, preserves a drainage system bound by two major tectonic faults. A quantitative geomorphic analysis of the drainage system reveals 68 catchments, with channel steepness and knickpoint analysis of catchment-hosted palaeo-rivers showing that the landscape preserved a >2 Myr long period of transient tectonics. We interpret that this landscape records a punctuated uplift of the footwall of a major rift-related normal fault (Vette Fault) at the onset of rifting. The landscape was preserved by a combination of relatively rapid subsidence in the hangingwall of a younger fault (Øygarden Fault) and burial by post-incision sediments. As such, we show how and why erosional landscapes are preserved in the stratigraphic record, and how they can help us understand the tectono-stratigraphic evolution of ancient continental rifts.

KEYWORDS

drainage system, fault growth, geomorphology, North Sea, seismic reflection data, transient tectonics

1 | INTRODUCTION

Tectonics, landscape evolution and stratigraphy are closely coupled in active continental rifts (e.g., Allen, 2008; Cowie et al., 2000; Gawthorpe & Leeder, 2000; Pechlivanidou et al., 2017). Growing normal faults influence the geometry of drainage networks and incision rates within upland catchments (e.g., Kirby & Whipple, 2012; Roda-Boluda & Whittaker, 2017), which in turn controls the location, magnitude and routing of sediment supply to neighbouring depocenters (e.g., Burov & Poliakov, 2001; Cowie et al., 2006; Buiter et al., 2008; Bialas & Buck, 2009;

Olive et al., 2014; Andrés-Martínez et al., 2019). This coupling of tectonics, erosion and sedimentation (e.g., Olive et al., 2022; Romans et al., 2016; Watkins et al., 2020) means that the transient erosional response of fluvial landscapes to rifting can be used to record the timescales, throw rates and kinematics of active faulting over a range of spatial scales (e.g., Goren et al., 2014; Kirby & Whipple, 2012; Whittaker & Boulton, 2012; Zondervan et al., 2020). In modern rifts, we can analyse digital elevation models (DEMs), together with independent tectonic and stratigraphic constraints, to estimate the patterns and rates of fault evolution (e.g., Pechlivanidou et al., 2017; Quye-Sawyer et al., 2021; Watkins et al., 2020), but in many ancient rifts, similar rift-related palaeo-landscapes are absent. Consequently, time-averaged patterns of faulting must be reconstructed indirectly from structural measurements and stratigraphic observations (e.g., Gawthorpe & Leeder, 2000; Kent et al., 2017). If palaeo-landscapes can be found in the stratigraphic record of ancient rifts, they may reveal important new information about fault growth and evolution as landscapes can record tectonic forcing over timescales of 10^5 to 10^6 years (Whittaker & Boulton, 2012).

To our knowledge, the oldest reported 3D buried palaeo-landscapes are 55–58 Ma seismically imaged drainage networks offshore Scotland, UK, developed and preserved in response to Iceland plume-driven uplift and subsidence (Hartley et al., 2011; Shaw-Champion et al., 2008; Stucky de Quay et al., 2017). Here, we present an even older mountainous landscape, defined by an erosional surface carved into the Palaeozoic basement of the northern North Sea rift, offshore Norway, imaged in 3D seismic reflection data. The surface covers at least 542 km² and reveals a drainage system that developed at the onset of Permian–Triassic rifting (ca. 261 ± 10 Ma; Fossen & Dunlap, 1999). A quantitative geomorphic analysis of the surface shows that this drainage system contains an exceptional record of the transient landscape response to faulting, from which we deduce the history and timescales of rift-related normal fault evolution. Our work therefore shows how palaeo-surfaces imaged in 3D seismic reflection data can provide crucial insights into the tectonostratigraphic evolution of ancient continental rifts.

2 | GEOLOGICAL SETTING

The study area is located in the northern North Sea rift, offshore Norway (Figure 1a). An up to 12-km-thick syn- and post-rift sedimentary succession was deposited on the crystalline basement during and after Late Permian-Early Triassic and Middle Jurassic-Early Cretaceous rifting (Bell et al., 2014; Færseth, 1996; Maystrenko et al., 2017). In the

Highlights

- Here we present a candidate for the oldest complete 3-D landscape described from the geological record; an erosional surface carved into the Paleozoic basement of the northern North Sea rift, offshore Norway.
- The surface covers at least 542 km² and reveals a drainage system that developed at the onset of Permian-Triassic rifting (ca. 261 ± 10 Ma).
- A quantitative geomorphic analysis of the surface shows that this drainage system contains an exceptional record of the transient landscape response to incipient faulting, from which we deduce the history and timescales of rift-related normal faulting.

Late Permian-Early Triassic, E-W extension led to the development of large (>100 km long in some cases) normal faults, such as the W-dipping Tusse, Vette and Øygarden faults, which bound half-grabens and are the focus of this study (Figure 1a,b). By the Triassic, these faults had developed large displacements (up to 4 km, measured as the distance between hanging and footwall cut-offs of stratigraphic horizons) and were associated with relatively high slip rates (0.1–0.15 mm/yr; Bell et al., 2014); however, the relative age of these faults and the order in which they initiated remains unknown. The top of the basement in the footwall of the Vette Fault constitutes a distinct erosional surface (Figure 1b), which we describe and analyse in further detail below. The surface is carved into 'basement' rocks, which are interpreted to consist of Devonian sedimentary rocks, Caledonian allochthons and Proterozoic crystalline rocks based on the onshore geology and limited offshore boreholes penetrating acoustic basement (Fazlikhani et al., 2017). From the few wells that penetrate the sediments above the top basement surface, we know that it is capped by upper Permian rocks composed of unfossiliferous desert sandstones overlain by carbonates and evaporites formed under extreme climate conditions and Early Triassic rocks are comprised of continental redbed intervals deposited in alluvial-fan, fluvial, flood-basin and lacustrine environments (Evans, 2003), which we interpret as good evidence that the surface was formed by subaerial erosion.

3 | DATA

The 3D pre-stack depth-migrated seismic data (provided courtesy of CGG) used in this study were acquired with a
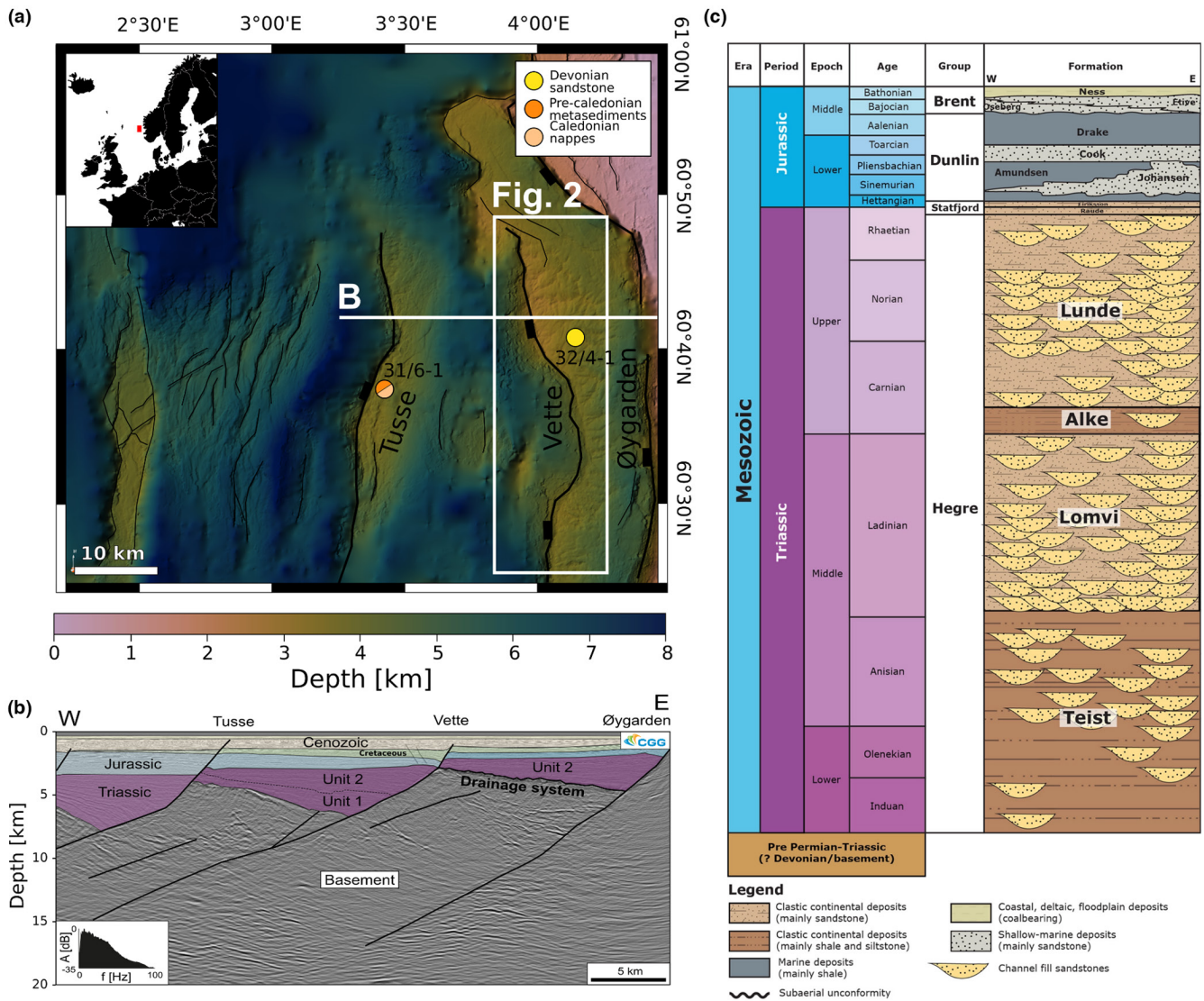
FIGURE 1 (a) Map view of the interpreted basement surface showing rift-related normal faults and drainage system in the northern North Sea. (b) Seismic section (depth-migrated) shows the drainage systems situated on top of the basement. Permian–Triassic strata overlying the surface consist of two wedge-shaped units. Seismic data courtesy of CGG. Note that the depth migration has been calibrated with borehole checkshots. (c) West–east chronostratigraphic chart for the Permian-middle Jurassic in the Horda platform (from Würtzen et al., 2021). Modified from NPD (https://npd.no/en/facts/geology/lithostratigraphy/). Lithostratigraphy is illustrated in the right column with an emphasis on mud versus sand-dominated intervals. The applied stratigraphic nomenclature is in accordance with the revised scheme by Lervik (2006).

G-Gun array consisting of 3 subarrays with a source array depth of 6–9 m—a source length of 16–18 m—a shot point interval of 18.75 m—a source separation of 37.5 m—a volume of $0.07456\,m^3$ and an air pressure of $1.379 \times 10^7\,Pa$. The streamer consisted of 12 up to 8-km-long cables with 636 channels each; a cable separation of 75 m and group spacing of 12.5 m; depths of 7–50 m covering offsets of 150–8100 m. The data were recorded with a 2 ms sample interval, 9000 ms recording length, a low cut filter (2 Hz–6 db/oct) and a high cut (200 Hz–370 db/oct) filter.

The seismic data were processed in 90 steps including divergence compensation, a low cut filter (1.5, 2.5 Hz),

noise attenuation (e.g., swelling, direct wave), spatial anti-aliasing filter (12.5 m group interval), direct wave attenuation, source de-signature, de-spike, a time-variant high cut filter, receiver motion correction and de-ghosting, FK filter, cold water and tidal statics, multiple modelling with adaptive subtraction, Tau-P mute, Radon de-multiple, far angle de-striping, multiple attenuations, binning (75 m interval, 107 offset planes), acquisition hole infill, 5D regularisation, 3D true amplitude Kirchhoff pre-stack depth migration, residual move-out correction, Linear FL Radon, full offset stack with time-variant inner and outer mute, acquisition footprint removal, cross-line K

filter, residual de-striping and dynamic Q-compensation. The seismic volume was zero phases processed with SEG normal polarity (peaks are white and troughs are black in seismic images). The data were depth converted using a velocity model calibrated using borehole checkshots. This results in a vertical seismic resolution (a quarter of the wavelength) of ca. 18 m at the depth of interest (ca. 4 km).

4 | METHODS AND RESULTS

In this section, we outline the steps required to recover rift evolution from ancient landscapes as well as present the fundamental methods. We also outline in this section the key findings from the application of each step. In the next section, we integrate these findings to reveal the landscape response to faulting.
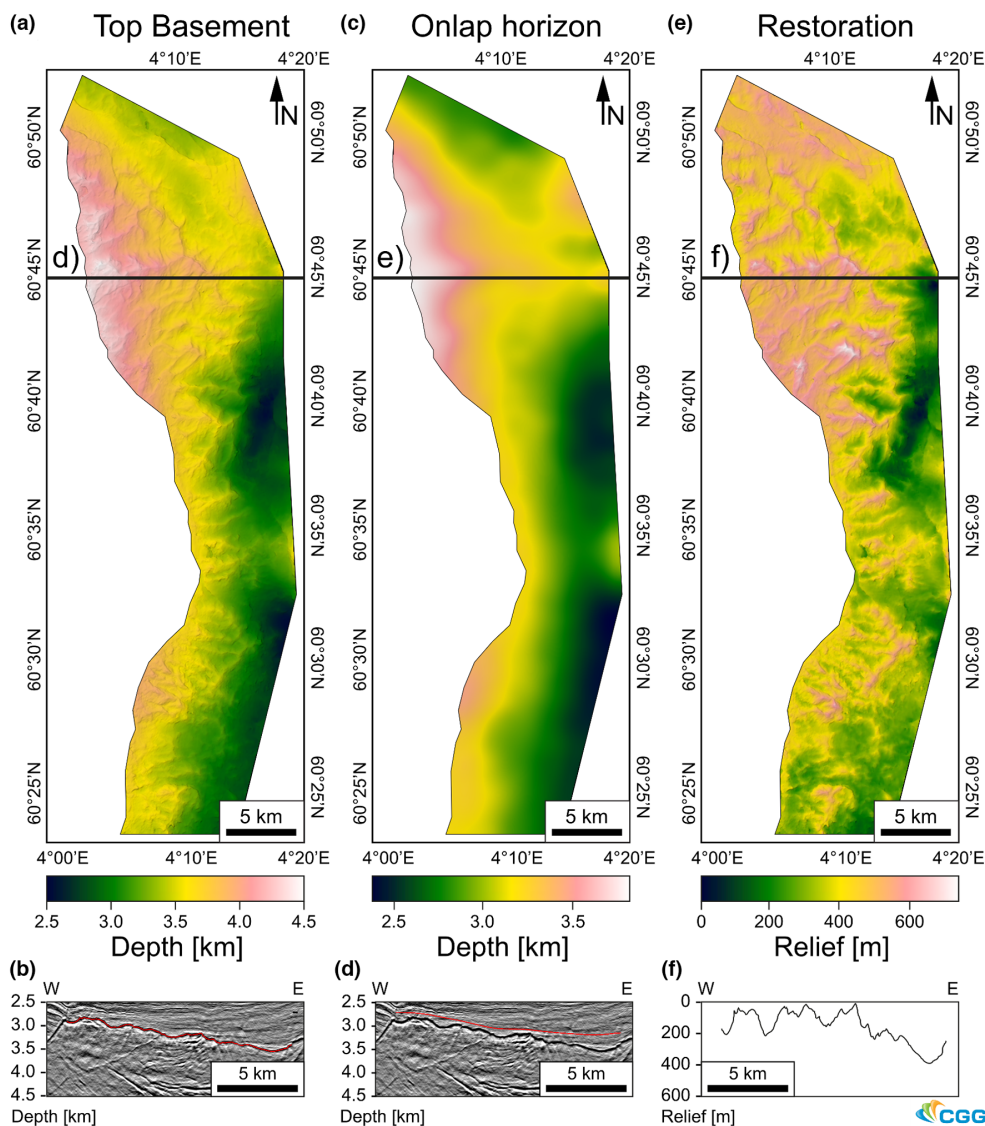
4.1 | Seismic interpretation

We mapped the top of the acoustic basement at a spatial resolution (i.e., bin size) of 12.5 × 18.5 m, revealing a palaeo-landscape preserved in the footwall of the Vette Fault (Figure 1). The top of the acoustic basement is a high-amplitude normal polarity reflection originating from the impedance contrast between sedimentary rocks (above) and crystalline basement (below). In cross-section, the top basement surface is highly irregular, showing relatively steep slopes (up to 15°) and moderate relief (<800 m) (Figure 1b). In plan view, the erosional surface mapped from the seismic data (Figure 2a) reveals an intricate 3D landscape showing a small fault-bounded mountain range with relief up to 800 m, incised by a dendritic fluvial network, from which individual catchments can be identified with exceptional clarity, particularly in the north of the area (Figure 2a). The fault block into which the landscape is carved is bound by two major tectonic normal faults (the Øygarden and Vette faults), which we map using fault plane reflections and cut-offs of footwall and hanging wall strata (Figures 1b and S1). We also map two wedge-shaped, likely Permian–Triassic units (Units 1 and 2) overlying the crystalline basement, which allows us to (i) infer the timing of landscape formation and preservation and (ii) better understand the processes leading to the preservation of the studied landscape. The oldest strata (Unit 1) is defined by medium-to-low amplitude, continuous, sub-horizontal reflections and only occurs in the hanging wall of the Vette Fault, thinning westwards from 2.2 km immediately adjacent to the Vette Fault to 0.3 km on the footwall crest of the Tusse Fault. This thinning towards the Vette Fault can be seen explicitly in the depth of the paleo-surface onlap horizon

within Unit 1 shown in Figure 2b. The younger, overlying unit, Unit 2, is defined by low-amplitude, discontinuous reflections and is also present in the hanging wall of the Vette Fault, but it is also developed in the hanging wall of the Øygarden Fault (i.e., it caps the footwall of the Vette Fault) (Figure 1b). The wedge-shaped geometries of units 1 and 2 suggest that they were deposited during active normal faulting, that is they are syn-tectonic. Although no wells penetrate these wedges directly, we estimate their age as Permian–Triassic based on the correlation of seismic reflections from areas where sediment age is constrained by drilling (e.g. Bell et al., 2014; Færseth, 1996; Heeremans & Faleide, 2004).

4.2 | Top basement restoration

To analyse the original geomorphology of this top basement surface, we created a DEM by restoring the top basement to its original geometry (cf. Hartley et al., 2011; Stucky de Quay et al., 2017) (Figure 2). First, we mapped the top basement surface (Figure 2a,b) and the first continuous onlap horizon overlying it (Figure 2c,d). Because this onlap horizon shows almost no topography, we can assume that it once was a more-or-less horizontal palaeo-surface. By subtracting the depth of this onlap surface from the basement surface, we can obtain an approximation of the basement morphology at the time of formation of the onlap surface (Figure 2e,f). We can then grid the basement surface, so it becomes a digital elevation model (DEM) with a cell size of 50 × 50 m. This reduction in spatial sampling smooths the topography and removes seismic artefacts. We note, however, that this simple restoration method does not account for any tilting that occurred between the development of the paleo-landscape and the deposition of the onlap surface. Given the fact this paleo-landscape lies in the hanging wall of the Permian–Triassic active Øygarden fault, it is expected that some tilting occurred during the deposition of the sediments between the basement and onlap surface.

Quantitative geomorphic analyses based on the basement surface DEM produced by simply subtracting the onlap surface from the basement surface produced some anomalous drainage patterns, including catchments draining internally or away from the Vette Fault (i.e., to the East) (Figure 3). This suggested, as we expected, that a small degree of tilting between exposure of the landscape and deposition of the onlap surface had occurred. After testing a range of rotations, we found that tilting the surface by 3° to the west, relative to the Vette Fault, was enough to remove the effect of eastward fault block rotation prior to onlap, producing more realistic looking drainage catchments (Figure 3D). Consequently, we

FIGURE 2 (a) Top basement surface showing the drainage system. (b) Seismic section showing the surface interpretation. (c) Onlap horizon (smoothed). (d) Seismic section showing the horizon onlapping onto the top basement surface. (e) Top basement surface minus the onlapping horizon to restore original morphology. (f) Profile of restored basement relief along the seismic section. Seismic data courtesy CGG. Note that the effect of compaction could not be accounted for due to uncertainties in the host rock properties controlling compaction.

proceed below using the palaeo-surface DEM with this 3° correction applied.

4.3 | Geomorphic analysis

To recover the evolution of the Vette and Øygarden faults that cut the basement surface and control the ancient drainage surface, we performed a quantitative geomorphic analysis. Such analyses are much more and commonly performed on modern systems, where different topographic models can be compared and where properties such as precipitation rate, river discharge and bedrock strength can be well constrained (e.g., Crosby & Whipple, 2006; DiBiase et al., 2014; Goren et al., 2014;

Kent et al., 2021; Smith et al., 2022; Whittaker et al., 2007 and references therein). Here, we cannot measure or estimate bedrock erodibility (or changes thereof), because the surface is buried under 4 km of sedimentary strata and the basement rocks, into which the surface is eroded are not fully characterised (Fazlikhani et al., 2017). Similarly, although the climate appears to have been consistently arid during late Permian-early Triassic times (e.g., Würtzen et al., 2021), there are no reliable estimates of precipitation rates for that time interval. Consequently, the geomorphic analysis of buried landscapes is by necessity more limited than what can be achieved with modern topographies. Although we cannot analyse the effects of these variables on the surface, we can still (1) extract a drainage network from the surface, (2) analyse channel steepness variations,

Structural restoration
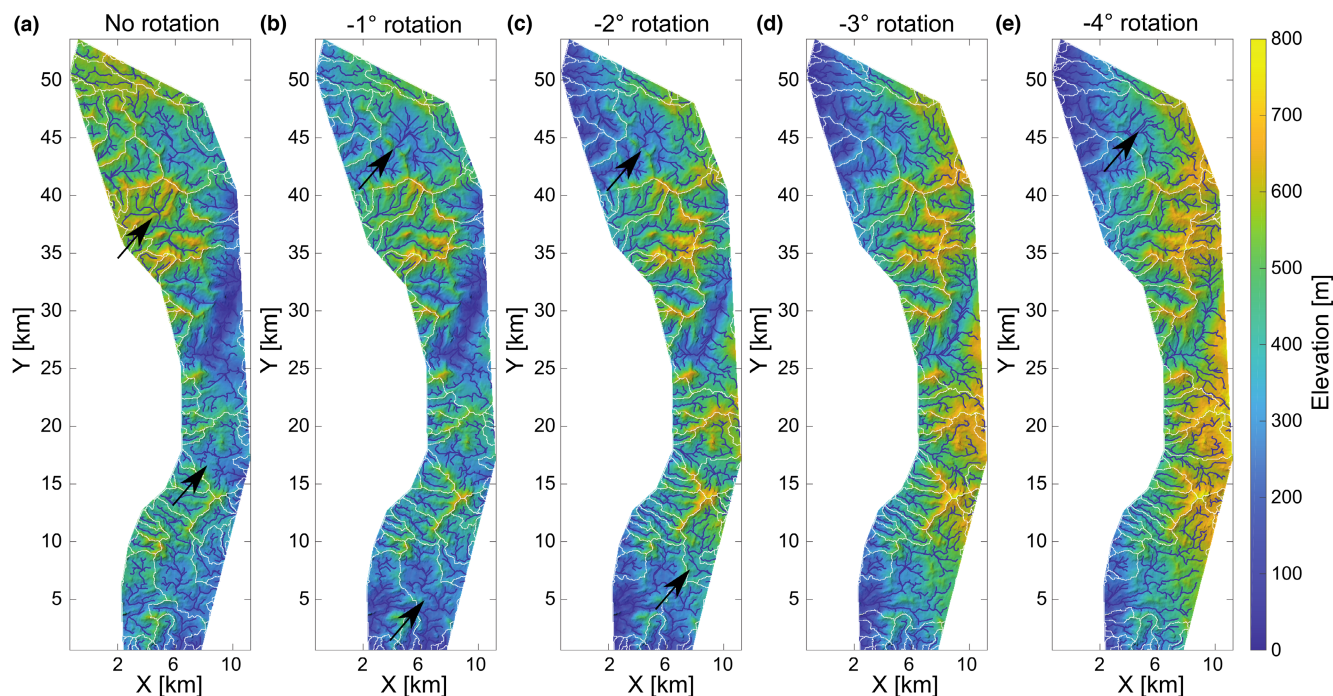
FIGURE 3 Basement surface with stream network and drainage divides restored for different degrees of fault block rotation (0–4°). A moderate rotation of 3° results in a realistic stream network (d). Note that catchments at the edge of the surface could extend beyond. Arrows indicate unrealistic drainage patterns resulting from incorrect rotation angles.

(3) extract knickpoints from river elevation profiles (where present) and (4) estimate a range of knickpoint migration times. These steps help us to understand the evolution of the palaeo-landscape as well as give unique insights into the history of the Vette and Øygarden faults at the beginning of Permian–Triassic rifting.

4.3.1 | Stream network extraction

To analyse the drainage network, we first extract it from the restored basement surface DEM using TopoToolbox 2 (Schwanghart & Scherler, 2014). First, we fill the DEM to remove any erroneous elevation values to generate a consistent hydrological surface (Figure 4). As the maximum filling depth, we select the seismic resolution (18 m, i.e., quarter of the wavelength at the depth of interest) of our data set (Figure 4b). Our ancillary analysis of filling depth sensitivity shows that when this value is too high, river networks are straightened and begin to show unrealistic geometries (Figure 4d,e). Next, we recover stream networks and river-long profiles using a D8 flow routing algorithm with a flow accumulation threshold of 0.25 km² typically used in modern systems (e.g., Whittaker & Boulton, 2012) (Figure 5e). This threshold corresponds to the minimum area draining into one cell belonging to a river. If this value is too low, we introduce

an unrealistically large number of first-order tributaries (Figure 5a–c).

#### 4.3.1.1 | *Channel steepness calculation*

To highlight deviations in channel gradient with respect to the fault, we calculate the normalised channel steepness across our network. River incision upstream of active faults is often well described by a family of stream power erosion 'laws' (Kirby & Whipple, 2012; Tucker & Whipple, 2002; Whittaker et al., 2007; Whittaker & Walker, 2015). In these cases, channel slope (S) is related to the upstream drainage area (A) by a power law, which would imply that rivers in the topographic steady state exhibit a concave up profile that represents a balance between a downstream increase in discharge and the downstream decrease in channel gradient. For a classic stream power model, where a river is in the topographic steady state (i.e., erosion rate = uplift rate), we can write:

$$S = \left(\frac{U}{K}\right)^{\frac{1}{n}} A^{\frac{-m}{n}}, \tag{1}$$

where U represents a rock uplift rate (e.g., driven by faulting), K is a coefficient that describes a number of factors modulating the efficiency of erosion (e.g., bedrock erodibility) and m and n are positive exponents which are related to both the long-term erosional dynamics of the system and

Topographic filling
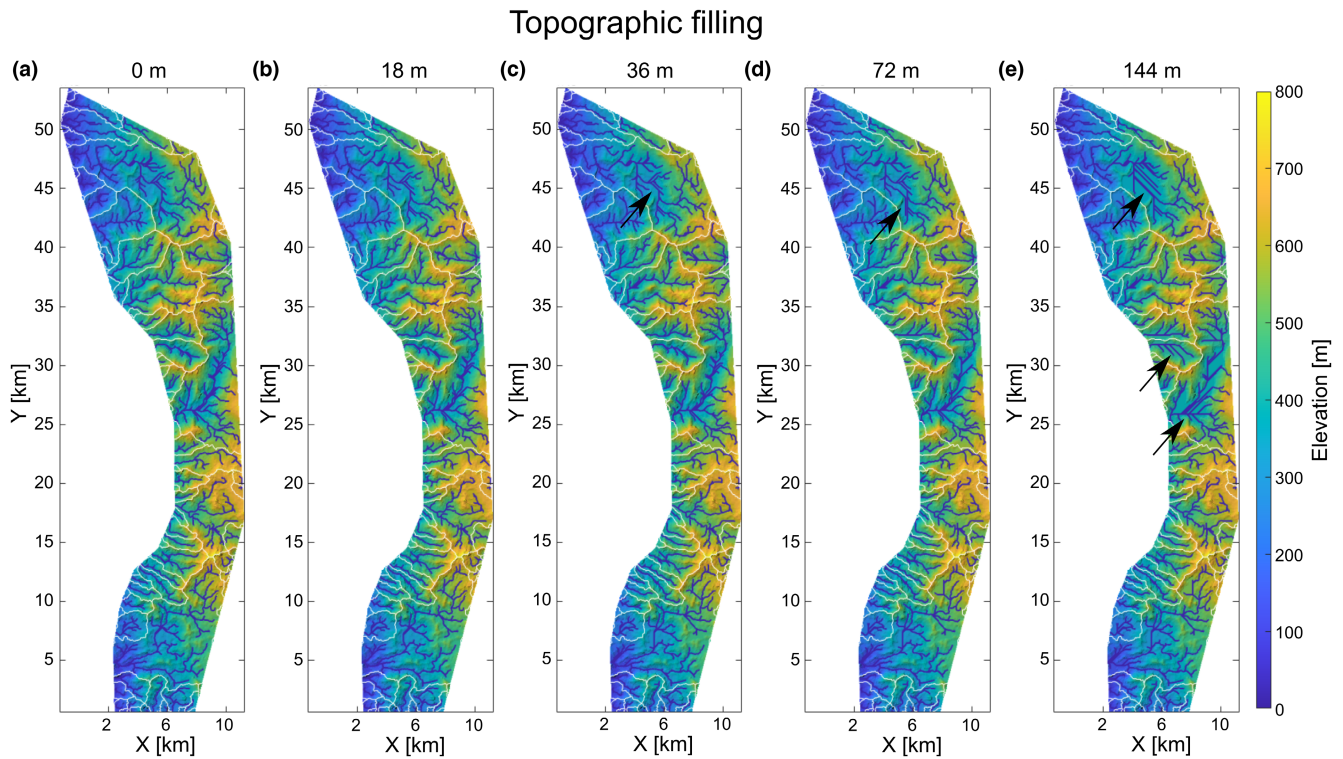
FIGURE 4 Basement surface with stream network and drainage divide for different amounts of topographic filling. Note that high filling values result in straightened streams and rivers. To remove erroneous elevation values, we use the seismic resolution of 18 m (b) as the maximum filling depth of the DEM. Note that unrealistically high filling values result in the artificial straightening of rivers and streams (see arrows).

Flow accumulation threshold
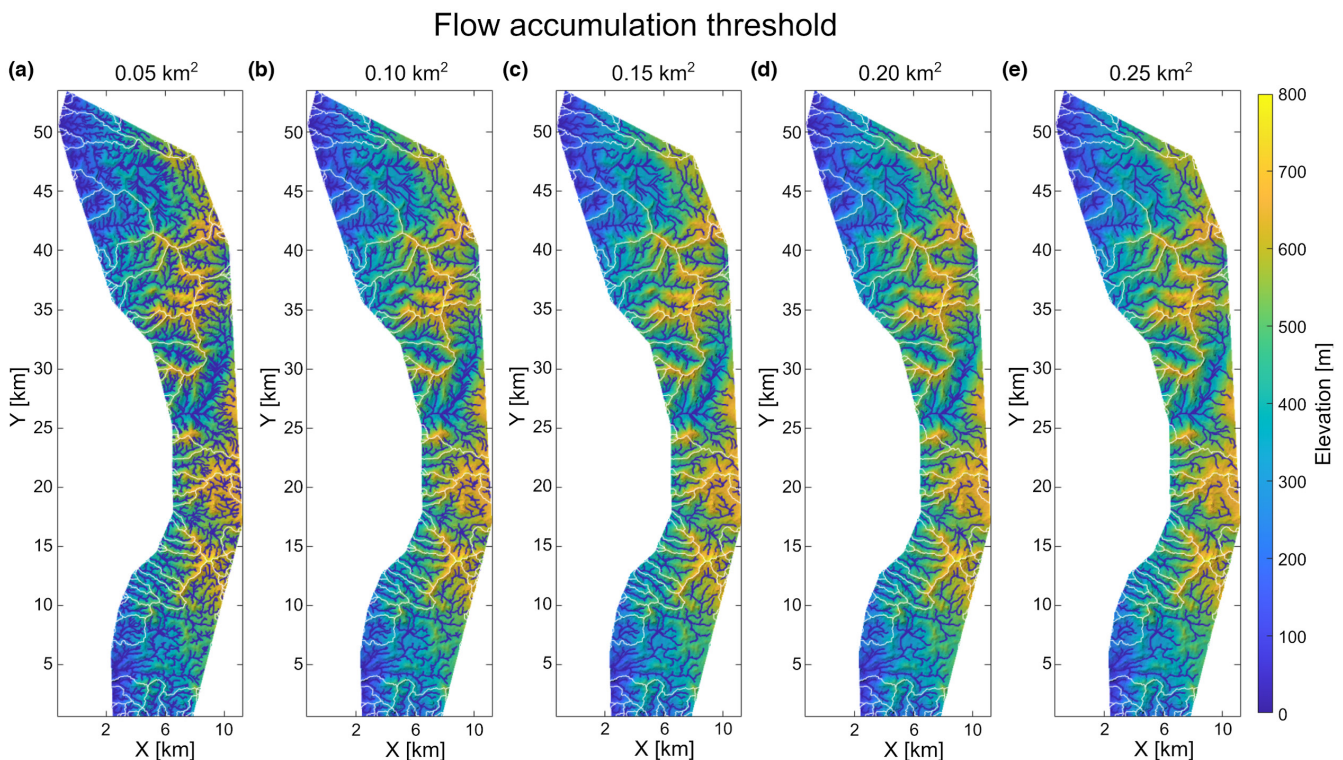
FIGURE 5 Basement surface with stream network and drainage divide for different flow accumulation cut-offs. Note that low cut-off values result in more tributaries. We chose a flow accumulation threshold of 0.25 km^2 (e) typically used in modern systems (e.g., Whittaker & Boulton, 2012). Note that low flow accumulation thresholds (e.g., 0.05, 0.1) result in unrealistic drainage networks consisting of a large number of extremely small streams.

its hydraulic geometry (e.g., Kirby & Whipple, 2012). From Equation (1), we can derive

$$ksn = \left(\frac{U}{K}\right)^{\frac{1}{n}} \qquad (2)$$

This term represents the channel steepness index (ksn), which can be calculated from the slope (S) and the upstream drainage area (A) as well as the coefficients m and n, which control the channel concavity (θ), where

$$\theta = \frac{m}{n} \qquad (3)$$

A reference value of θ is often used to estimate a normalised channel steepness index, ksn, allowing comparisons between channels with different concavities (e.g., Gailleton et al., 2021; Snyder et al., 2000; Wobus et al., 2006). Given a global mean concavity index for channels of 0.45 (Schwanghart & Scherler, 2014), and the fact that $\theta = 0.45$ is commonly used in many other comparable studies, we calculate normalised channel steepness along our stream network using this value (e.g., Roda-Boluda & Whittaker, 2017; Wobus et al., 2006).

4.3.1.2 | Knickpoint extraction

Knickpoints in individual catchments can be generated by a range of processes including base level change, rock strength variations and landslide (e.g., Scheingross et al., 2021). However, the presence of large profile convexities (knickpoints) located consistently in footwall catchments upstream of active normal faults very often reflects the transient response of fluvial systems to relative base level change such as a change in fault slip rate (e.g., Whittaker et al., 2007; Kent et al., 2021; Quye-Sawyer et al., 2021). In this scenario, the river reaches downstream of a knickpoint, but for instance upstream of an active fault, has steepened and incised in response to the tectonic perturbation, while upstream of the knickpoint has yet to respond to the fault-driven uplift and retains its pre-existing configuration (Kirby & Whipple, 2012). Knickpoints migrate upstream over time, eventually transmitting the relative tectonic perturbation throughout the catchment area over timescales of 10^6 years or more (Harkins et al., 2007; Tucker & Whipple, 2002; Whittaker & Boulton, 2012). In this context, we identify knickpoints in the palaeo-river long profiles of our stream network using the knickpoint finder of TopoToolbox 2 (Schwanghart & Scherler, 2017). The knickpoint finder works by reconstructing the measured river elevation profile iteratively. During each iteration, the finder removes a constraint on the curvature at the locations with the maximum offset between the measured and reconstructed profile. After a few iterations, the vertical offset decreases

to a minimum tolerance set by the user (Figures 6 and 7). Because this tolerance should reflect vertical uncertainty in the data (Schwanghart & Scherler, 2017), we use 2.5 times the seismic resolution of our survey (45 m; Figure 6c). This high tolerance assures that we extract only major knickpoints in the network (Figure 7c). While other knickpoints may arguably be identified in the data by inspection, we do not pick knickpoints manually to ensure that our results are robust and reproducible.

After the extraction, we measure the elevation of these knickpoints relative to the Vette Fault (where it cuts the river) to a precision of ± 25 m, and their distance upstream with a precision of ± 100 m (Table 2). Knickpoint height relative to the fault is compared to geological constraints on fault throw (cf. Bell et al., 2014), and knickpoint locations are compared to palaeo-catchment drainage area.

4.3.1.3 | Knickpoint migration time estimation

For any knickpoints located upstream of the footwall-bounding Vette Fault and interpreted to be generated by tectonic forcing, we estimate a timescale for their propagation upstream, assuming they started from the fault, using an estimated propagation velocity V, derived from a unit stream power erosion law (Tucker & Whipple, 2002; Whittaker & Boulton, 2012):

$$V \simeq KA^m S^{1-n}. \qquad (4)$$

For these calculations, we assume that n is 1, as this is tractable and simple to first order. Moreover, past studies explicitly investigating footwall catchments upstream of active normal faults have indicated that $1 - n$ is a reasonable approximation, based on observations of discharge-constrained unit stream powers scaling with fault throw rates (e.g., Kent et al., 2021; Whittaker & Boulton, 2012; Zondervan et al., 2020). We acknowledge that the true value of n in stream power erosion laws applied to modern systems is much discussed in the literature (e.g., Lague, 2014). However, it is not possible to constrain n independently for this 250 Ma old landscape, so we argue $n = 1$ involves the fewest assumptions, and that it is better to privilege a simpler model over a more complex one. Similarly, if we assume $m - 0.5$, which is broadly consistent with global concavity values, we obtain a very simple dimensional relationship between the velocity of knickpoint retreat, V, and the drainage area, A, where K has units of the inverse of time:

$$V \simeq KA^{0.5} \qquad (5)$$

This equation means that migration rates decrease as knickpoints propagate upstream along rivers from the fault, and drainage areas upstream of the knickpoints reduce (e.g., Crosby & Whipple, 2006; DiBiase et al., 2014;
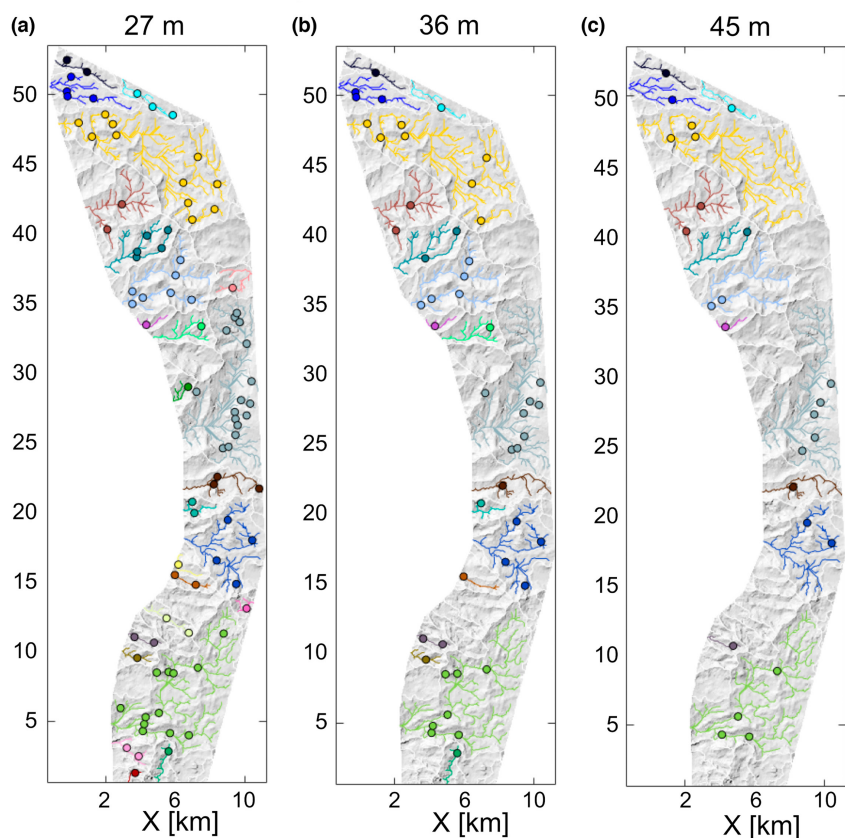
Knickpoint finder tolerance
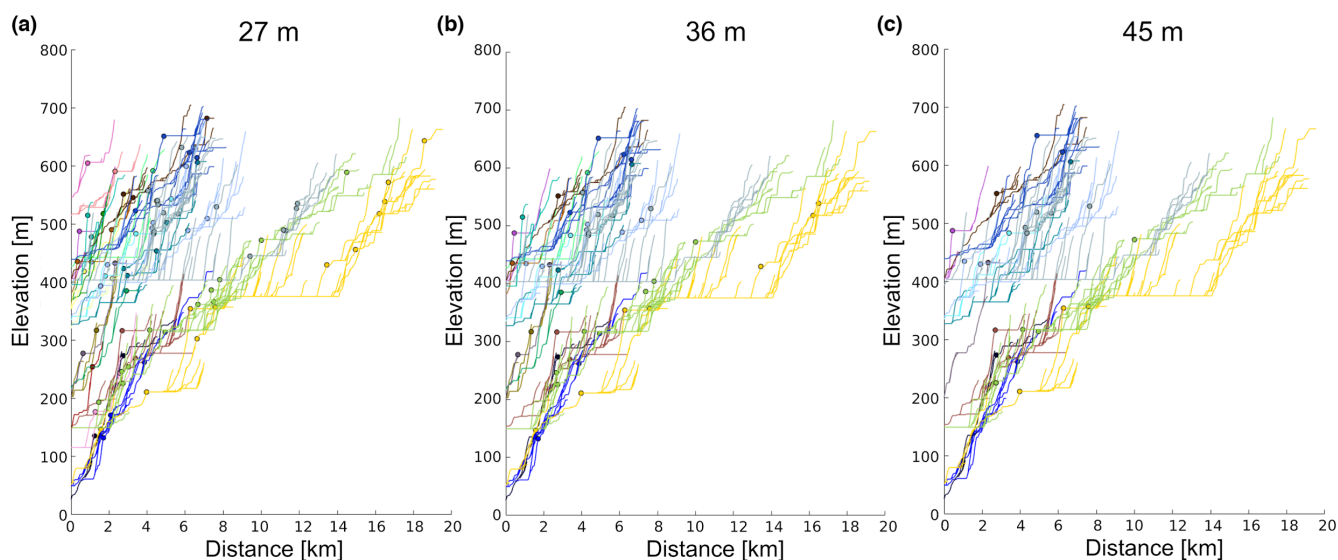
Knickpoint finder tolerance

FIGURE 7   Knickpoints along elevation profiles extracted for different tolerance values of (a) 27, (b) 36 and (c) 45 m.

Goren et al., 2014; Mitchell & Yanites, 2019). In our case, we can capture this effect by computing the speed and distance the knickpoints can propagate from the fault, given the known length of the trunk channels with respect to their known drainage area at any point in the fluvial network. We can therefore estimate knickpoint migration time by stepwise summation of the product of the migration distance as a function of velocity-dependent drainage area as long as we have an estimate of K. We choose to use a range of values for K for the calculation of knickpoint

TABLE 1 Geomorphological data extracted from the analysed drainage network

Paleo-catchment number	River length (km)	Catchment area (km^2)
1	7.44	9.9
2	0.44	0.44
3	1.49	1.76
4	5.49	4.82
5	0.29	0.5
6	20.35	60.02
7	1.94	3.44
8	2.93	5.09
9	6.62	18.27
10	1.00	1.36
11	7.15	13.08
12	0.07	0.23
13	18.41	55.83
14	3.61	4.25
15	1.26	1.72
16	1.04	1.02
17	3.16	5.63
18	2.26	1.73
19	0.31	0.28
20	0.05	0.29
21	0.12	0.17
22	2.51	3.17
23	5.84	5.2
24	9.56	25.03
25	3.08	2.64
26	1.71	1.02
27	0.24	0.47
28	1.81	1.28
29	0.12	0.38
30	2.43	2.93
31	6.06	5.3
32	4.64	3.55
33	0.45	0.47
34	5.17	8.54
35	3.67	8.63
36	5.45	3.64
37	4.79	8.43
38	0.81	0.8
39	0.17	0.2
40	0.42	0.53
41	3.92	3.13
42	3.31	3.15
43	0.70	0.59
44	2.09	0.42
45	0.26	2.71

(Continues)

TABLE 1 (Continued)

Paleo-catchment number	River length (km)	Catchment area (km^2)
46	3.21	4.62
47	1.95	1.34
48	14.45	50.7
49	0.05	0.34
50	0.05	0.23
51	3.17	3.38
52	7.63	10.13
53	2.87	3.68
54	1.23	1.04
55	1.92	1.62
56	8.20	23.8
57	0.19	0.23
58	5.48	1.02
59	1.63	0.94
60	3.82	0.58
61	0.63	12.52
62	2.35	0.37
63	0.79	6.31
64	1.87	2.06
65	0.53	0.38
66	0.10	2.57
67	0.66	0.91
68	1.17	0.89

migration times taken directly from the knickpoint data compilation presented in Whittaker and Boulton (2012). These data show that for rivers of similar size to the catchments, we consider here and crossing active normal faults with comparable slip rates in both Italy and Turkey, 0.5×10^{-6} yr$^{-1} < K < 2 \times 10^{-6}$ yr^{-1} (Whittaker & Boulton, 2012). We stress that this analysis aims to give a first-order estimate of knickpoint propagation rates and landscape response times. The use of larger or smaller values of this variable would scale calculated knickpoint migration times accordingly. Note that these calculations neglect the isostatic effect of unloading as the amount of the bedrock exhumation is not known.

4.4 | Landscape response to active faulting at ca. 250 Ma

From this unique palaeo-landscape and from our sensitivity analyses in Figures 3–7, we extracted 68 palaeo-catchments with drainage areas up to 60 km^2 and longest trunk rivers of up to 20 km, which we analyse below (Table 1; Figure 8). Many catchments show abrupt channel steepness index variations (Figure 8b).

Significantly, high steepness index river segments (>50 m long) are mainly found in catchments that decrease in elevation and appear to drain westwards towards the Vette Fault (Figure 8b). Reconstructed palaeo-channel long profiles are *not* concave up but show distinct convexities on a range of length scales (Figure 8c,d). The channel long profiles are remarkably similar to those observed in modern fluvial systems draining across active normal faults (e.g., Goren et al., 2014; Kent et al., 2021; Whittaker & Boulton, 2012). Consequently, the sharp variations in channel steepness suggest that the palaeo-landscape was not in a topographic steady state when it was buried under stratigraphic units 1 and 2.

We extract 25 knickpoints from the palaeo-river long profiles we obtain from our preferred DEM (Figure 8a,c,d; Table 2). Thirteen catchments have at least one significant knickpoint upstream of the Vette Fault and several have two. These knickpoints lie at distances between 0.44 and 10 km upstream of the Vette Fault, with elevations for the lower or single set of knickpoints varying between 45 and 300 m above the elevation where they cross the Vette Fault (Figure 8d). In terms of their size and scale, these catchments and knickpoints are directly comparable to modern fluvial systems crossing normal faults in Italy, Turkey, and Greece (Fernandez-Blanco et al., 2019; Kent et al., 2021; Roda-Boluda & Whittaker, 2017; Whittaker & Walker, 2015), where rivers have been shown to record changing fault slip rates over timescales of 1–5 million years.

When plotted along the strike of the Vette Fault (Figure 9c), the elevation of the knickpoints relative to the fault (i.e., the height of the knickpoint above the fault where it intersects the river downstream) is an order of magnitude smaller than the fault throw obtained from Bell et al. (2014) between 0 and 40 km along strike, with these values being comparable for the northern part of the fault between 40 and 60 km (Figure 9). Knickpoint elevations are smallest 25–40 km along strike, which is where the throw is presently greatest (Figure 9b,c). The majority of catchments crossing the fault have one knickpoint (red circles); some have two knickpoints identified (white circles). The upper set of knickpoints also have elevations that are considerably less than the geologic throw. Given that knickpoints can be created by a change in relative base level caused by faulting, such as an increase in fault slip rate, and given that knickpoint elevation, since formation, is known to scale predictably with fault slip rate (cf. Tucker & Whipple, 2002; Whittaker et al., 2008; Wobus et al., 2006), we deduce that the knickpoints are related to the active faulting which was happening at the time. Further, we infer for those knickpoints located to the east of the southern part of the Vette Fault, that they likely post-date the accumulation of some of the slip on the fault as their elevations are much less than the footwall relief of the paleo-surface (e.g., Whittaker & Walker, 2015). However, these knickpoints also clearly pre-date subsequent throw on the fault accumulated during the deposition of Units 1 and 2 (Bell et al., 2014), which we show to bury the landscape (Figure 1). We also note that
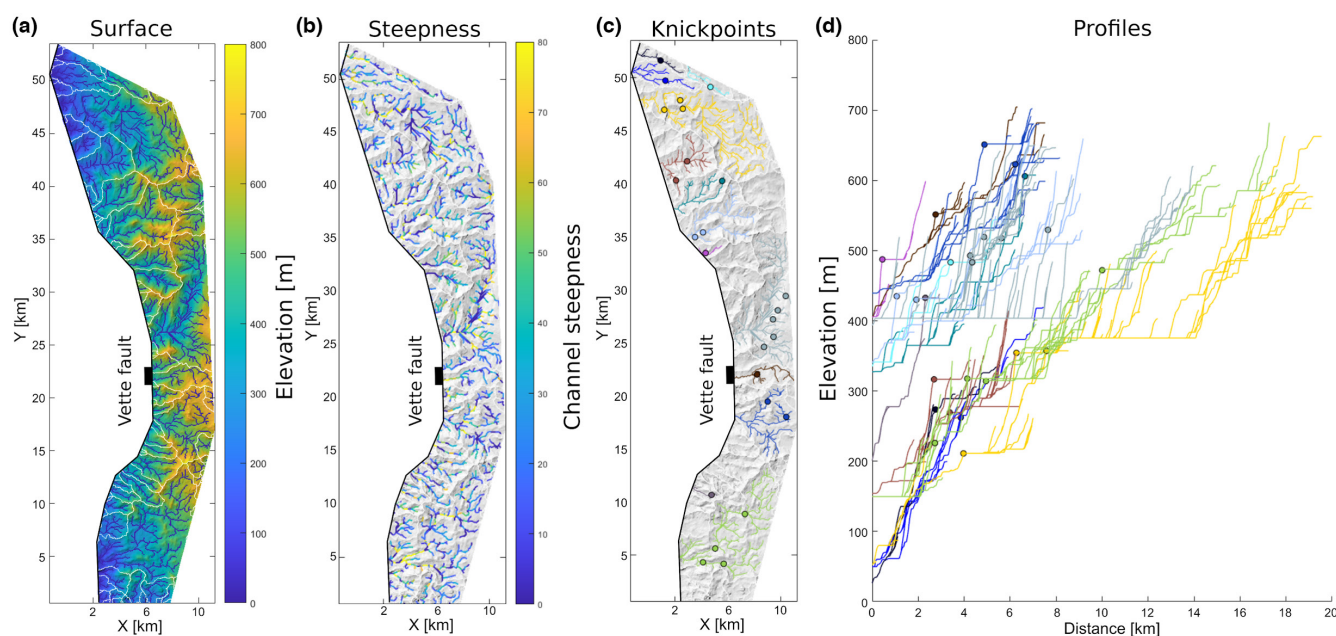
FIGURE 8 (a) Best-fit restored basement surface with stream network and drainage divides. (b) Normalised channel steepness index of the stream network. (c) Knickpoints in map view extracted from stream network and used in our analysis. (d) Knickpoint elevations along long profile extracted from our stream network shown in (c).

TABLE 2 Knickpoint migration distance extracted from drainage network. Migration times were calculated with $K = [0.5, 1.0, 2.0] * 10^6$ from Whittaker and Boulton (2012)

| Knickpoint number	Height (m)	Downstream area (km²)	Distance from Vette fault (km)	Low K landscape response time (Myr)	Medium K landscape response time (Myr)	High K landscape response time (Myr)	Low K migration time (Myr)	Medium K migration time (Myr)	High K migration time (Myr)
1	158	3.71	6.27	2.49	4.99	9.98	1.33	2.67	5.34
2	51	1.89	3.85	1.43	2.87	5.73	0.82	1.64	3.28
3	96	3.94	2.75	1.42	2.85	5.7	0.71	1.43	2.85
4	59	1.81	3.97	2.49	4.99	9.98	1	2.01	4.01
5	85	11.02	2.69	0.93	1.86	3.71	0.32	0.63	1.27
6	52	4.27	6.64	1.22	2.44	4.88	1.16	2.32	4.64
7	108	2.91	4.13	1.68	3.37	6.74	0.58	1.17	2.33
8	50	0.28	3.41	1.58	3.16	6.31	1	2.01	4.01
9	56	1.33	1.07	1.21	2.42	4.84	0.34	0.69	1.37
10	60	0.05	2.31	0.69	1.37	2.75	0.65	1.29	2.59
11	64	5.9	0.44	1.44	2.87	5.75	0.71	1.42	2.82
12	75	1.9	4.86	1.44	2.87	5.75	0.59	1.18	2.35
13	45	5.95	2.76	1.5	3.01	6.01	0.48	0.97	1.93
14	89	0.62	4.88	1.15	2.3	4.6	0.69	1.38	2.77
15	55	14.37	3.37	0.93	1.86	3.71	0.54	1.07	2.15
16	49	6.12	7.58	2.49	4.99	9.98	0.47	0.93	1.86
17	65	0.92	4.95	1.68	3.37	6.74	0.85	1.71	3.41
18	50	25	1.92	1.21	2.42	4.84	0.14	0.29	0.57
19	73	7.89	10	1.68	3.37	6.74	0.95	1.9	3.79
20	59	9.67	5.62	1.44	2.87	5.75	0.69	1.39	2.78
21	48	2.32	6.22	1.15	2.3	4.6	0.95	1.9	3.81
22	45	4.54	2.73	1.68	3.37	6.74	0.43	0.87	1.74
23	58	0.68	4.26	1.44	2.87	5.75	1.37	2.74	5.49
24	48	4.73	7.64	1.44	2.87	5.75	0.84	1.68	3.35
25	46	0	4.35	1.44	2.87	5.75	1.29	2.57	5.14

along-strike changes in elevation appear to cluster into two zones, separated by low knickpoint point heights relative to the fault at approximately 30 km along the fault strike. These results resemble the distribution of knickpoints mapped upstream of modern fault segments (e.g., Roda-Boluda & Whittaker, 2017; Whittaker & Walker, 2015) so we infer the existence of two palaeo-fault segments (south: 0–30 km and north: 30–60 km) that were likely active early in the evolution of the Vette Fault—we explore this further in our discussion below.

Although there is considerable scatter, knickpoints on palaeo-catchments with bigger drainage areas are generally located further upstream (L – A$^{0.38\pm0.12}$) (Figure 10). If all the knickpoints had been generated at a single time, for instance by a single fault linkage event that increased fault slip rate, we would expect the distance they had propagated to scale predictably with ca. A0.5 assuming similar values for K for all rivers (cf. Whittaker & Walker, 2015). The spread of data therefore suggests that the knickpoints we have documented were likely generated by more than one event, but several of them may have formed within a similar time window given that those located on big catchments are in some cases located predictably further upstream from the fault. Overall, we interpret these knickpoints to capture the transient response of the footwall landscape to the early growth of the Vette Fault near the onset of Permian–Triassic rifting. The palaeo-landscape was subsequently buried in the hanging wall of the Øygarden Fault before the transient tectonic signal had a chance to propagate fully through the fluvial system.

5 | DISCUSSION

5.1 | Duration of faulting and knickpoint migration

Once formed, tectonically driven knickpoints migrate upstream, as catchments progressively respond to the relative change in base level (Kirby & Whipple, 2012). We can thus use the vertical and plan view position of the knickpoints relative to the fault documented in this study as a proxy for the timescale of fault growth and the transient landscape response to this. Knickpoint elevation upstream of interacting fault segments is known to scale with the relative rate of base level changes and the time since this has taken place (Whittaker & Boulton, 2012). The maximum elevation of the lower knickpoints is ca. 250 m. If we divide this by published throw rates on the Vette Fault of 0.15 mm/yr (Bell et al., 2014) as a maximum, this would imply that the transient landscape represents a minimum of 1.7 Myr, similar to faulted landscapes in Greece (e.g., Whittaker & Walker, 2015). However, we do not have good constraints on fault throw rates in the early history of the Vette Fault, which may have been less than 0.15 mm/yr. Alternatively, we can calculate upstream migration rates of the knickpoints using plausible bedrock erodibilities based on an average of a compilation of modern systems upstream of active faults with similar drainage areas and slip rates (cf. 'Data and Methods; Whittaker & Boulton, 2012), we obtain timescales of knickpoint propagation of 0.14–5.49 Myr (Table 2; Figure 11). These imply a median landscape response time of 2.98 Myr and extremes of 0.69–9.98 Myr if
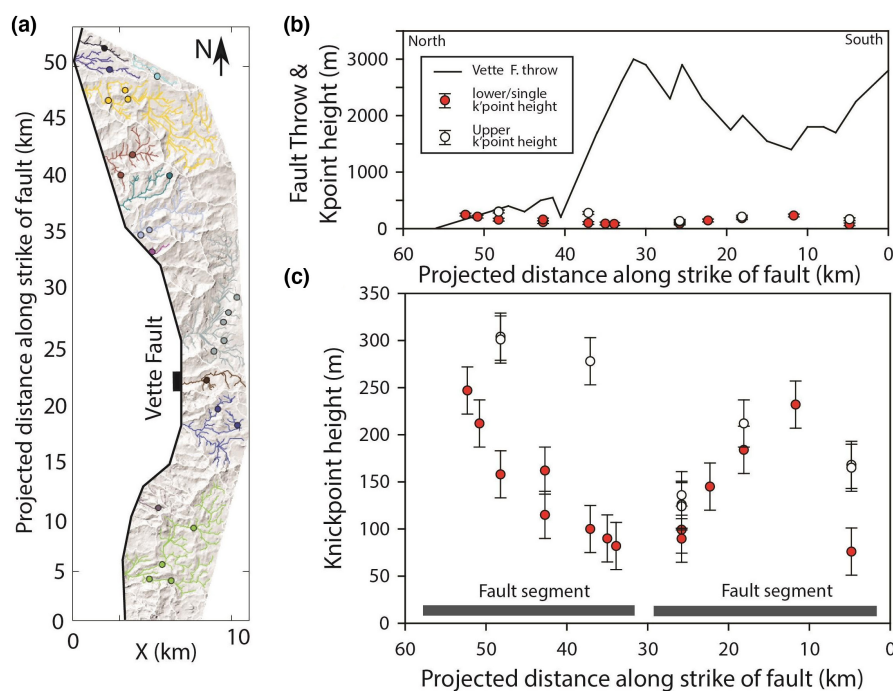
FIGURE 9 (a) Knickpoints extracted from stream network. (b) Knickpoint height and fault throw along strike (same scale). (c) Knickpoint height with error bar. Note the two populations of knickpoints (upper-white and lower-red). Knickpoint height refers to the height of the knickpoint above the fault where it intersects the river downstream.
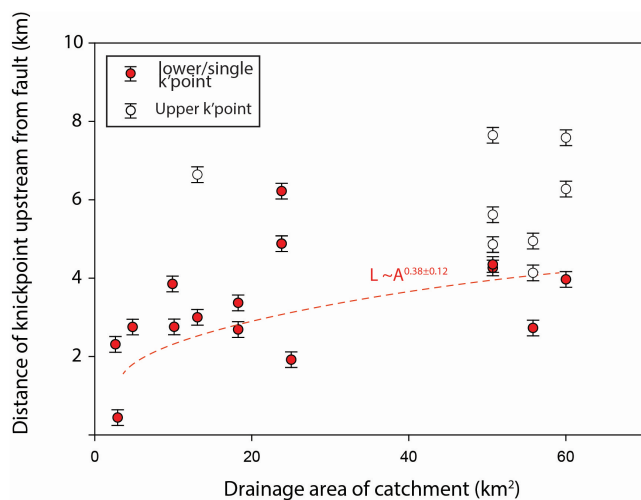
FIGURE 10 Distance of knickpoints upstream from the Vette Fault against catchment area for these knickpoints (i.e., integrated upstream area of the catchment from the fault to the knickpoint). The best-fit line for lower/single knickpoints is a power law.

we estimate the time taken for the knickpoints along strike to propagate to the headwaters of the catchments (i.e., $A < 1$ km^2) (Table 2). The consistency of these estimates for the vertical and plan view timescale of knickpoint propagation indicates these values are plausible and consequently we deduce that the palaeo-landscape records fault growth and interaction over a period of a few million years (Figure 4c). Considering that dating of sedimentary rocks, fault rocks and dykes suggests that Permian–Triassic rifting began around 261 ± 10 (Fossen & Dunlap, 1999) and lasted tens of millions of years (Fossen et al., 2021; Ravnås et al., 2000), our results indicate that the Vette Fault was only this active for a fraction of this episode. This analysis therefore demonstrates how geomorphic techniques can provide further detail on the timescales of ancient fault growth which cannot be obtained from deeply buried syn-rift sediments which commonly lack sufficient age control (cf. Cowie et al., 2006). This suggests that looking for palaeo-landscapes in other seismic data sets of rifted margins would be useful for constraining the timescales and history of fault growth in conjunction with conventional stratigraphic and structural analyses.

5.2 | Landscape preservation—Strain migration

A key question is how the palaeo-landscape we have reconstructed was generated, buried and preserved. To understand this question, we reconstruct the tectono-stratigraphic context and evolution of the fault and landscape system through time, which we summarise in Figure 12. Given that the landscape is buried underneath
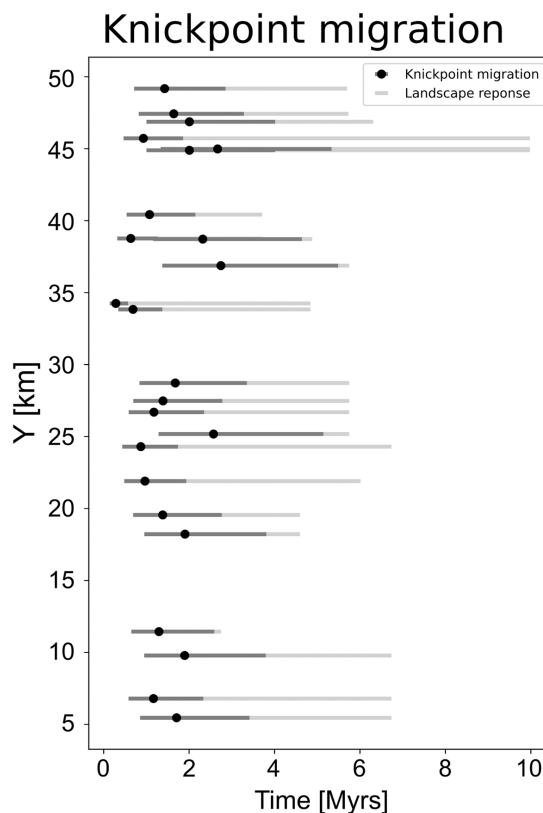
FIGURE 11 Knickpoint migration and landscape response time estimates for $K = [0.5, 1.0, 2.0] * 10^6$ from north to south.

a syn-tectonic (i.e., wedge-shaped) Permian–Triassic stratigraphic unit (Units 1 and 2), the landscape almost certainly developed during the onset of Permian–Triassic rifting in the northern North Sea. The underlying syn-tectonic (i.e., wedge-shaped) Permian–Triassic unit (Unit 1) formed in the hanging wall of the Vette Fault indicating that the fault was active when the landscape was at the surface (Figure 4a). At this time, there is no evidence that the neighbouring Øygarden Fault was active as Unit 1 is not found in its hangingwall, whereas Unit 2 thickens markedly towards this structure (Figure 12a). The knickpoints and overall landscape we have documented were created when early segments of the Vette Fault were actively creating footwall topography and displacing palaeo-streams and rivers—these segments subsequently grew together and potentially linked, increasing fault slip rates as they did so (Figure 2c) (see also Bell et al., 2014). Our analysis shows that the landscape upstream of the Vette Fault at this stage was not in a topographic steady state, and that the knickpoints we document record a time period of 0.14–5.49 Myr, the drainage system was rapidly subsided (but not below sea level), buried and preserved beneath sub-aerial Permian–Triassic strata (Unit 2) which also thickens towards the Øygarden Fault (Figures 1b and 4b). The rapid burial of the footwall of the Vette Fault, before the transient landscape had equilibrated, was likely
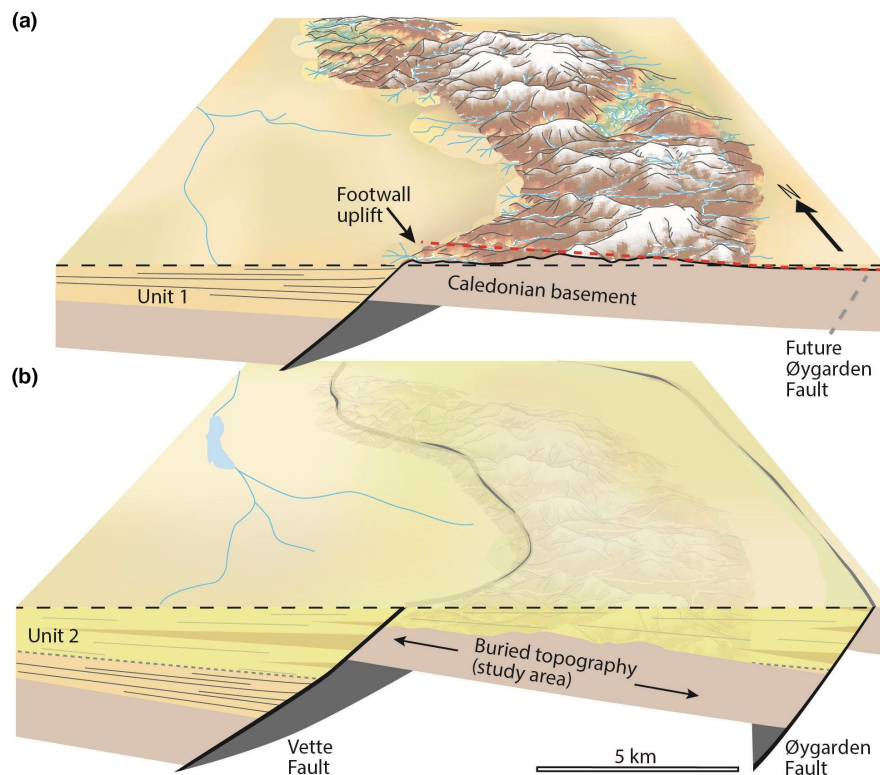
FIGURE 12 3D diagram illustrating landscape evolution at the onset of rifting. (a) landscape development at the onset of rifting in the northern North Sea, when the young Vette fault initiated and Permian–Triassic strata (unit 1) were being deposited in its immediate hanging wall. Knickpoints creation when segments of the Vette fault were displacing palaeo-streams and rivers as they grew, interacted and built footwall relief. (b) subsequent subsidence and rapid burial underneath Permian–Triassic strata (unit 2) leading to landscape preservation.

driven by strain migration from the Vette Fault to the larger Øygarden Fault during rift evolution on the eastern margin of the North Viking Graben. This interpretation is supported by the fact that the Øygarden Fault likely achieved a length of >100 km during the Permo-Triassic stage of rifting (Bell et al., 2014). Consequently, we hypothesise that the hanging wall of this fault produced subsidence rates that outpaced footwall uplift on the Vette Fault, leading to the rapid burial of the basement landscape (Figure 12b).

6 | CONCLUSIONS

This study reveals a sub-aerial drainage system carved into the basement surface of the northern North Sea Rift. This system covers at least 542 km² and is bound by two major tectonic normal faults, the Øygarden Fault to the East and the Vette Fault to the West. A quantitative geomorphic analysis of the system reveals that many catchments draining across the Vette Fault have high (>60) steepness indices and that 13 of the 68 catchments have knickpoints indicating that the landscape preserved a

period of transient tectonics driven by footwall uplift of the Vette Fault at the onset of Late Permian-Early Triassic rifting (ca. 250 Ma). Two independent estimates based on published fault slip and knickpoint migration rates suggest that the palaeo-landscape records fault growth and interaction over periods of a few million years. Finally, we interpret that this landscape was preserved by an eastward shift of fault activity from the Vette to the Øygarden Fault, effectively subsiding and burying the landscape beneath Permian–Triassic strata (Unit 2) in the hanging wall of the Øygarden Fault.

PEER REVIEW

The peer review history for this article is available at https://publons.com/publon/10.1111/bre.12732.

DATA AVAILABILITY STATEMENT

Research data cannot be shared due to the economic interests of the data provider (CGG).

ORCID

Thilo Wrona [ID] https://orcid.org/0000-0002-9707-0595
Alexander C. Whittaker [ID] https://orcid.org/0000-0002-8781-7771
Rebecca E. Bell [ID] https://orcid.org/0000-0002-4785-9707
Robert L. Gawthorpe [ID] https://orcid.org/0000-0002-4352-6366
Haakon Fossen [ID] https://orcid.org/0000-0002-8091-5643
Christopher A.-L. Jackson [ID] https://orcid.org/0000-0002-8592-9032

REFERENCES

Allen, P. A. (2008). From landscapes into geological history. *Nature*, *451*(7176), 274–276. https://doi.org/10.1038/nature06586

Andrés-Martínez, M., Pérez-Gussinyé, M., Armitage, J., & Morgan, J. P. (2019). Thermomechanical implications of sediment transport for the architecture and evolution of continental rifts and margins. *Tectonics*, *38*, 641–665.

Bell, R. E., Jackson, C. A.-L., Whipp, P. S., & Clements, B. (2014). Strain migration during multiphase extension: Observations from the northern North Sea. *Tectonics*, *33*(10), 1936–1963. https://doi.org/10.1002/2014TC003551

Bialas, R. W., & Buck, W. R. (2009). How sediment promotes narrow rifting: Application to the Gulf of California. *Tectonics*, *28*, TC4014.

Buiter, S. J. H., Huismans, R. S. C., & Beaumont, C. (2008). Dissipation analysis as a guide to mode selection during crustal extension and implications for the styles of sedimentary basins. *Journal of Geophysical Research*, *113*, B06406.

Burov, E. B., & Poliakov, A. N. B. (2001). Erosion and rheology controls on synrift and postrift evolution: Verifying old and new ideas using a fully coupled numerical model. *Journal of Geophysical Research*, *106*, 16461–16481.

Cowie, P. A., Attal, M., Tucker, G. E., Whittaker, A. C., Naylor, M., Ganas, A., & Roberts, G. P. (2006). Investigating the surface process response to fault interaction and linkage using a numerical modelling approach. *Basin Research*, *18*(3), 231–266. https://doi.org/10.1111/j.1365-2117.2006.00298.x

Cowie, P. A., Gupta, S., & Dawers, N. H. (2000). Implications of fault array evolution for synrift depocentre development: Insights from a numerical fault growth model. *Basin Research*, *12*(3–4), 241–261. https://doi.org/10.1046/j.1365-2117.2000.00126.x

Crosby, B. T., & Whipple, K. X. (2006). Knickpoint initiation and distribution within fluvial networks: 236 waterfalls in the Waipaoa River, North Island, New Zealand. *Geomorphology*, *82*, 16–38. https://doi.org/10.1016/j.geomorph.2005.08.023

DiBiase, R. A., Whipple, K. X., Lamb, M. P., & Heimsath, A. M. (2014). The role of waterfalls and knickzones in controlling the style and pace of landscape adjustment in the western San Gabriel Mountains, California. *Geological Society of America Bulletin*, *127*, 539–559. https://doi.org/10.1130/B31113.1

Evans, D. (2003). *The Millennium Atlas: Petroleum Geology of the Central and Northern North Sea; [a Project of the Geological Society of London, the Geological Survey of Denmark and Greenland and the Norwegian Petroleum Society]*.

Færseth, R. B. (1996). Interaction of permo-triassic and jurassic extensional fault-blocks during the development of the northern North Sea. *Journal of the Geological Society*, *153*(6), 931–944. https://doi.org/10.1144/gsjgs.153.6.0931

Fazlikhani, H., Fossen, H., Gawthorpe, R. L., Faleide, J. I., & Bell, R. E. (2017). Basement structure and its influence on the structural configuration of the northern North Sea rift. *Tectonics*, *36*(6), 1151–1177. https://doi.org/10.1002/2017TC004514

Fernandez-Blanco, D., de Gelder, G., Lacassin, R., & Armijo, R. (2019). A new crustal fault formed the modern Corinth Rift. *Earth Science Reviews*, *199*, 102919. https://doi.org/10.1016/j.earscirev.2019.102919

Fossen, H., & Dunlap, W. J. (1999). On the age and tectonic significance of Permo-Triassic dikes in the Bergen-Sunnhordland region, southwestern Norway. *Norsk Geologisk Tidsskrift*, *79*(3), 169–177. https://doi.org/10.1080/002919699433807

Fossen, H., Ksienzyk, A. K., Rotevatn, A., Bauck, M. S., & Wemmer, K. (2021). From widespread faulting to localised rifting: Evidence from K-Ar fault gouge dates from the Norwegian North Sea rift shoulder. *Basin Research*, *33*, 1934–1953. https://doi.org/10.1111/bre.12541

Gailleton, B., Mudd, S. M., Clubb, F. J., Grieve, S. W. D., & Hurst, M. D. (2021). Impact of changing concavity indices on channel steepness and divide migration metrics. *Journal of Geophysical Research: Earth Surface*, *126*, e2020JF006060. https://doi.org/10.1029/2020JF006060

Gawthorpe, R. L., & Leeder, M. R. (2000). Tectono-sedimentary evolution of active extensional basins. *Basin Research*, *12*(3–4), 195–218. https://doi.org/10.1046/j.1365-2117.2000.00121.x

Goren, L., Fox, M., & Willett, S. D. (2014). Tectonics from fluvial topography using formal linear inversion: Theory and applications to the Inyo Mountains, California. *Journal of Geophysical Research: Earth Surface*, *119*(8), 1651–1681. https://doi.org/10.1002/2014JF003079

Harkins, N., Kirby, E., Heimsath, A., Robinson, R., & Reiser, U. (2007). Transient fluvial incision in the headwaters of the Yellow River, northeastern Tibet, China. *Journal of Geophysical Research: Earth Surface*, *112*(F3). https://doi.org/10.1029/2006JF000570

Hartley, R. A., Roberts, G. G., White, N., & Richardson, C. (2011). Transient convective uplift of an ancient buried landscape. *Nature Geoscience*, *4*(8), 562–565. https://doi.org/10.1038/ngeo1191

Heeremans, M., & Faleide, J. I. (2004). Late Carboniferous-Permian tectonics and magmatic activity in the Skagerrak, Kattegat and the North Sea. In M. Wilson, E.-R. Neumann, G. R. Davies, M. J. Timmermann, M. Heeremans, & B. T. Larsen (Eds.), *Permo-Carboniferous magmatism and rifting in Europe* (Vol. *223*, pp. 157–176). Geological Society Special Publications.

Kent, E., Boulton, S. J., Whittaker, A. C., Stewart, I. S., & Cihat Alçiçek, M. (2017). Normal fault growth and linkage in the

Gediz (Alaşehir) Graben, Western Turkey, revealed by transient river long-profiles and slope-break knickpoints. *Earth Surface Processes and Landforms*, *42*(5), 836–852. https://doi.org/10.1002/esp.4049

Kent, E., Whittaker, A. C., Boulton, S., & Alçiçek, M. (2021). Quantifying the competing influences of lithology and throw rate on bedrock river incision. *GSA Bulletin*, *133*(7–8), 1649–1664.

Kirby, E., & Whipple, K. X. (2012). Expression of active tectonics in erosional landscapes. *Journal of Structural Geology*, *44*, 54–75. https://doi.org/10.1016/j.jsg.2012.07.009

Lague, D. (2014). "The stream power river incision model: evidence, theory and beyond." *Earth Surface Processes and Landforms*, *39*(1), 38–61.

Lervik, K. (2006). "Triassic lithostratigraphy of the northern North Sea Basin." *Norsk Geologisk Tidsskrift*, *86*(2), 93.

Maystrenko, Y. P., Olesen, O., Ebbing, J., & Nasuti, A. (2017). Deep structure of the northern north sea and southwestern Norway based on 3D density and magnetic modelling. *Norsk Geologisk Tidsskrift*, *97*(3), 169–210. https://doi.org/10.17850/njg97-3-01

Mitchell, N. A., & Yanites, B. J. (2019). Spatially variable increase in rock uplift in the northern U.S. cordillera recorded in the distribution of river knickpoints and incision depths. *Journal of Geophysical Research: Earth Surface*, *124*(5), 1238–1260. https://doi.org/10.1029/2018JF004880

Olive, J.-A., Behn, M. D., & Malatesta, L. C. (2014). Modes of extensional faulting controlled by surface processes. *Geophysical Research Letters*, *41*, 6725–6733.

Olive, J. A., Malatesta, L. C., Behn, M. D., & Buck, W. R. (2022). Sensitivity of rift tectonics to global variability in the efficiency of river erosion. *Proceedings of the National Academy of Sciences*, *119*(13), e2115077119. https://doi.org/10.1073/pnas.2115077119850

Pechlivanidou, S., Cowie, P. A., Hannisdal, B., Whittaker, A. C., Gawthorpe, R. L., Pennos, C., & Riiser, O. S. (2017). Source-to-sink analysis in an active extensional setting: Holocene erosion and deposition in the Sperchios rift, Central Greece. *Basin Research*, *30*(3), 522–543. https://doi.org/10.1111/bre.12263

Quye-Sawyer, J., Whittaker, A. C., Roberts, G. G., & Rood, D. H. (2021). Fault throw and regional uplift histories from drainage analysis: Evolution of southern Italy. *Tectonics*, *40*(4). https://doi.org/10.1029/2020tc006076

Ravnås, R., Nøttvedt, A., Steel, R. J., & Windelstad, J. (2000). Syn-rift sedimentary architectures in the northern North Sea. *Geological Society Special Publication*, *167*, 133–177. https://doi.org/10.1144/GSL.SP.2000.167.01.07

Roda-Boluda, D. C., & Whittaker, A. C. (2017). Structural and geomorphological constraints on active normal faulting and landscape evolution in Calabria, Italy. *Journal of the Geological Society*, *174*(4), 701–720. https://doi.org/10.1144/jgs2016-097

Romans, B. W., Castelltort, S., Covault, J. A., Fildani, A., & Walsh, J. P. (2016). Environmental signal propagation in sedimentary systems across timescales. *Earth-Science Reviews*, *153*, 7–29. https://doi.org/10.1016/j.earscirev.2015.07.012

Scheingross, J. S., Repasch, M. N., Hovius, N., Sachse, D., Lupker, M., Fuchs, M., Halevy, I., Gröcke, D. R., Golombek, N. Y., Haghipour, N., & Eglinton, T. I. (2021). The fate of fluvially-deposited organic carbon during transient floodplain storage. *Earth and Planetary Science Letters*, *561*, 116822

Schwanghart, W., & Scherler, D. (2014). Short communication: TopoToolbox 2—MATLAB-based software for topographic analysis and modeling in Earth surface sciences. *Earth Surface Dynamics*, *2*(1), 1–7. https://doi.org/10.5194/esurf-2-1-2014

Schwanghart, W., & Scherler, D. (2017). Bumps in river profiles: Uncertainty assessment and smoothing using quantile regression techniques. *Earth Surface Dynamics*, *5*(4), 821–839. https://doi.org/10.5194/esurf-5-821-2017

Shaw-Champion, M. E., White, N. J., Jones, S. M., & Lovell, J. P. B. (2008). Quantifying transient mantle convective uplift: An example from the Faroe-Shetland basin. *Tectonics*, *27*, TC1002. https://doi.org/10.1029/2007TC002106

Smith, A. G. G., Fox, M., Schwanghart, W., & Carter, A. (2022). Comparing methods for calculating channel steepness index. *Earth-Science Reviews*, *227*, 103970. https://doi.org/10.1016/j.earscirev.2022.103970

Snyder, N. P., Whipple, K. X., Tucker, G. E., & Merritts, D. J. (2000). Landscape response to tectonic forcing: Digital elevation model analysis of stream profiles in the Mendocino triple junction region, northern California. *Bulletin of the Geological Society of America*, *112*(8), 1250–1263. https://doi.org/10.1130/0016-7606(2000)112<1250:LRTTFD>2.0.CO;2

Stucky de Quay, G., Roberts, G. G., Watson, J. S., & Jackson, C. A. L. (2017). Incipient mantle plume evolution: Constraints from ancient landscapes buried beneath the North Sea. *Geochemistry, Geophysics, Geosystems*, *18*(3), 973–993. https://doi.org/10.1002/2016GC006769

Tucker, G. E., & Whipple, K. X. (2002). Topographic outcomes predicted by stream erosion models: Sensitivity analysis and intermodel comparison. *Journal of Geophysical Research: Solid Earth*, *107*(B9), ETG 1-1–ETG 1-16. https://doi.org/10.1029/2001jb000162

Watkins, S. E., Whittaker, A. C., Bell, R. E., Brooke, S. A., Ganti, V., Gawthorpe, R. L., McNeill, L. C., Nixon, C. W., & Stephen Watkins, C. E. (2020). Straight from the source's mouth: Controls on field-constrained sediment export across the entire active Corinth rift, Central Greece. *1600 | Basin Research*, *32*, 1600–1625. https://doi.org/10.1111/bre.12444

Whittaker, A. C., Attal, M., Cowie, P. A., Tucker, G. E., & Roberts, G. (2008). Decoding temporal and spatial patterns of fault uplift using transient river long profiles. *Geomorphology*, *100*(3–4), 506–526. https://doi.org/10.1016/j.geomorph.2008.01.018

Whittaker, A. C., & Boulton, S. J. (2012). Tectonic and climatic controls on knickpoint retreat rates and landscape response times. *Journal of Geophysical Research: Earth Surface*, *117*(F2). https://doi.org/10.1029/2011JF002157

Whittaker, A. C., Cowie, P. A., Attal, M., Tucker, G. E., & Roberts, G. P. (2007). Bedrock channel adjustment to tectonic forcing: Implications for predicting river incision rates. *Geology*, *35*(2), 103–106. https://doi.org/10.1130/G23106A.1

Whittaker, A. C., & Walker, A. S. (2015). Geomorphic constraints on fault throw rates and linkage times: Examples from the Northern Gulf of Evia, Greece. *Journal of Geophysical Research F: Earth Surface*, *120*(1), 137–158. https://doi.org/10.1002/2014JF003318

Wobus, C., Whipple, K. X., Kirby, E., Snyder, N., Johnson, J., Spyropolou, K., Crosby, B., & Sheehan, D. (2006). Tectonics from topography: Procedures, promise, and pitfalls. *Special Paper of the Geological Society of America*, *398*, 55–74. https://doi.org/10.1130/2006.2398(04)

Würtzen, C., Osmond, J., Faleide, J. I., Nystuen, J. P., Anell, I. M., & Midtkandal, I. (2021). Syn- to post-rift alluvial basin fill: Seismic stratigraphic analysis of Permian–Triassic deposition in the Horda platform, Norway. *Basin Research*, *4*, 1. https://doi.org/10.31223/X5K32G

Zondervan, J., Whittaker, A. C., Bell, R., Watkins, S., Brooke, S., & Hann, M. (2020). New constraints on bedrock erodibility and landscape response times upstream of an active fault. *Geomorphology*, *351*, 106937.

SUPPORTING INFORMATION

Additional supporting information can be found online in the Supporting Information section at the end of this article.